RSC Advances

PAPER

View Article Online
View Journal | View Issue

Cite this: *RSC Adv.*, 2022, **12**, 15751

High-performance self-supporting $AgCoPO_4$/CFP for hydrogen evolution reaction under alkaline conditions†

Wan Zhao,‡ Hongshuai Cao,‡ Liting Ruan, Shaoying He, Zhiai Xu and Wen Zhang *

Electrochemical water decomposition to produce hydrogen is a promising approach for renewable energy storage. It is vital to develop a catalyst with low overpotential, low cost and high stability for hydrogen evolution reaction (HER) under alkaline conditions. Herein, we used a simple hydrothermal method to obtain a $AgCo(CO)_4$ precursor on the surface of carbon fiber paper (CFP). After thermal phosphorization, the self-supporting catalyst $AgCoPO_4$/CFP was obtained, which greatly improved the HER catalytic performance under alkaline conditions. At 10 mA cm^{-2}, it showed an overpotential of 32 mV. The Tafel slope was 34.4 mV dec^{-1}. The high catalytic performance of $AgCoPO_4$/CFP may be due to the hydrophilic surface promoting effective contact with the electrolyte and the synergistic effect of the two metals, which accelerated electron transfer and thus promoted hydrogen evolution reaction. In addition, it showed an outstanding urea oxidation reaction (UOR) activity. After adding 0.5 M urea, the overpotential of the $AgCoPO_4$/CFP assembled electrolytic cell was only 1.45 V when the current density reached 10 mA cm^{-2}, which was much lower than that required for overall water splitting. This work provides a new method for the design and synthesis of efficient HER electrocatalysts.

Received 25th April 2022
Accepted 10th May 2022

DOI: 10.1039/d2ra02621j

rsc.li/rsc-advances

1. Introduction

Fossil fuel usage can produce carbon dioxide and other greenhouse gases, which are not friendly to the environment.[1,2] Sustainable production of hydrogen is important for developing green energy.[3–5] Electrocatalytic hydrogen evolution reaction (HER) is a crucial step in water splitting, which has been extensively studied in the last few decades.[6,7] As with any other chemical reaction, an energy input is required to overcome the electrochemical process of producing hydrogen from water. Preparing catalysts with excellent catalytic activity to optimize the catalytic performance and reduce the overpotential is the key step for water splitting.[8,9]

Generally, platinum-based catalysts and their derivatives[10,11] have the best hydrogen binding energy (HBE) and Gibbs free energy (ΔG_H^*),[12,13] however, precious metal catalysts in electrocatalytic HER have some disadvantages such as low reserves and high price.[14–16] Therefore, the development of efficient, economic and long-life catalyst is the key factor to realize high-performance energy storage.[17] Phosphate has attracted great attention because of its special structure and catalytic performance.[18] Xiao reported a novel heterostructures named $Co(PO_3)_2$@NPC/MoS_2, where NPC was N-doped porous carbon.[19] It clearly indicated that its electronic structure and HER performance was greatly ameliorated by interface of $Co(PO_3)_2$@NPC/MoS_2. In consequence, a lower overpotential of 119 mV was acquired in alkaline electrolyte at 10 mA cm^{-2}. However, catalysts synthesized by transition metals alone have limitations in reducing overpotential and maintaining stability. Various precious metal nanoparticles (such as Pt,[20] Ru,[21,22] Ir,[23,24] Au,[25] and Ag[26]) usually combined with transition metal-based catalysts to improve HER catalytic performance. Among them, silver-based electrocatalysts have outstanding performance due to their low price and abundant natural reserves.[27] Xu's group[28] prepared layered and porous Ag/Ag_2S heterostructures. Ag^+ acted as a regulator that competed with CoS linkers to control crystal growth rates and nucleation, adjusting pore size from micropore to macropore to achieve efficient mass transfer and to produce fully exposed active surfaces in porous frames. Thus, a better alkaline HER effect could be obtained. Therefore, combining the catalytic activity of noble metal with the stability of transition metal can effectively develop high-performance electrocatalysts.[29–31]

Herein, in order to solve the problems of high overpotential and poor stability of HER catalyst, hydrophilic $AgCo(CO)_4$/CFP precursor was synthesized by hydrothermal synthesis on hydrophobic carbon fiber paper (CFP) and $AgCoPO_4$/CFP was obtained after thermal phosphorization. Compared with CFP

School of Chemistry and Molecular Engineering, East China Normal University, Shanghai 200241, China. E-mail: wzhang@chem.ecnu.edu.cn

† Electronic supplementary information (ESI) available. See https://doi.org/10.1039/d2ra02621j

‡ W. Zhao and H. Cao contributed equally to this work.

and $AgCo(CO)_4$/CFP, $AgCoPO_4$/CFP had more favorable wettability, which can effectively contact the electrolyte and accelerate the reaction kinetics process. The synergistic effect of bimetal can accelerate the transmission of electrons and optimized the surface electronic structure of catalyst. Thus, the HER catalytic performance of $AgCoPO_4$/CFP was improved. In alkaline solution, the overpotential of $AgCoPO_4$/CFP was only 32 mV under the current density of 10 mA cm^{-2}, which was better than most non-noble metal-based catalysts. In addition, $AgCoPO_4$/CFP can perform HER catalysis for up to 25 h at a faint voltage of 32 mV at a current density of 10 mA cm^{-2}, showing excellent catalytic durability. The $AgCoPO_4$/CFP assembled electrolytic cell also obtained excellent catalytic performance.

2. Experimental section

2.1 Chemicals and materials

The chemicals and reagents are shown in ESI.†

2.2 Preparation of $AgCo(CO)_4$/CFP

The thickness of CFP is 0.19 mm (HCP121). CFP was cut into a size of 1 cm × 1.5 cm, ultrasonic cleaned in 30 mL hydrochloric acid for 10 minutes, then in ethanol for 20 minutes, at last it was dried for later use. The precursor $AgCo(CO)_4$/CFP was prepared by a hydrothermal process. At the beginning, a CFP piece was mixed with 40 mL of a solution containing 0.9 mmol $Co(NO_3)_2 \cdot 6H_2O$, 0.1 mmol $AgNO_3$, 5 mmol urea and 4 mmol NH_4F. The mixture was stirred for 5 h. Later, the solution including the CFP was heated up to 110 °C within a hydrothermal reactor for 10 h. After cooling naturally at room temperature, the crude product was washed with water and ethanol for 3 times. The precursor material produced by this hydrothermal reaction was known as $AgCo(CO)_4$/CFP.

2.3 Preparation of $AgCoPO_4$/CFP

$AgCoPO_4$/CFP was prepared from the precursor $AgCo(CO)_4$/CFP through a phosphorization step. At first, $AgCo(CO)_4$/CFP precursor and $NaH_2PO_2 \cdot H_2O$ (1.0 g) were respectively put in a porcelain boat. $NaH_2PO_2 \cdot H_2O$ was infixed into the tubular furnace and put it near the upstream side of the nitrogen gas flow. It was then heated to 380 °C in N_2 atmosphere and kept at this temperature for 3 h. We referred to the product after the phosphorization which was produced on the surface of CFP as $AgCoPO_4$/CFP. Note that the loading amount of the catalysts on CFP was around 0.6 mg cm^{-2} after the phosphorization process.

2.4 Electrochemical measurements

All the electrochemical measurements were carried out on Ingsens electrochemical workstation with a three-electrode system, in which a Hg/HgO electrode worked as the reference electrode, a carbon rod worked as the counter electrode and the catalyst was used as the working electrode. For comparison, HER was measured using Pt–C powder as the working electrode. Before electrochemical measurements, the electrolyte was absolutely eliminated dissolved gases by purifying with N_2 for 0.5 h. After stabilizing the current after 30 cycles of cyclic voltammetry (CV) tests, linear sweep voltammetry (LSV) with a scan rate of 5 mV s^{-1} was conducted in 1.0 M NaOH for HER. As for urea oxidation reaction (UOR), the measurements were measured in 1.0 M NaOH containing 0.5 M urea with the same scan rate. The *in situ* grown material was clamped with two electrode clips, and the contact area between the material and the electrolyte was 1.0 × 1.0 cm^2 as the anode and cathode of the working electrode in a single compartment as for overall water splitting. All measurements were based on the Nernst equation. The final potentials were calibrated to reversible hydrogen electrode (RHE): $E(\text{RHE}) = E(\text{Hg/HgO}) + 0.098V + 0.059 \times \text{pH}$. Double layer capacitances were acquired through CVs at different scan rates, from 100 to 420 mV s^{-1} in the potential range of −1.0 ∼ −0.6 V *vs.* RHE. The durability test was detected by a static over-potential for 25 h at −0.032 V in the cathode. During this time, the change of current with time was recorded.

3. Results and discussion

3.1 Structure and morphology characterization of as-prepared materials

As illustrated in Scheme 1, the solution of $Co(NO_3)_2$ and $AgNO_3$ was thoroughly stirred and placed with CFP within a hydrothermal reactor at 110 °C for 10 h to obtain precursor $AgCo(CO)_4$/CFP. $AgCo(CO)_4$/CFP was phosphorized to form the final $AgCoPO_4$/CFP with PH_3, which was generated *via* decomposition of $NaH_2PO_2 \cdot H_2O$.

X-ray diffraction (XRD) analysis was firstly used for material characterization. Fig. 1a showed the XRD pattern of the precursor. The composite exhibited a profile similar to the pattern of $AgCo(CO)_4$ with major diffraction peaks. After comparing with the PDF standard card, we found that the main peaks at 17.9°, 21.3°, 33.3° and 35.8° was corresponding to the (2 2 0), (−1 3 1), (0 6 1), and (−3 5 1) planes of $AgCo(CO)_4$ (PDF# 75-1810). In addition, the corresponding peaks of carbon fiber paper matched well with standard cards (PDF#75-2708). The morphology of the prepared product was then investigated by scanning electron microscope (SEM) (Fig. 1b and c). $AgCo(CO)_4$/CFP showed nanorod structure and the tip of the nanorods had large whiskers. In addition, the homogeneous distribution of $AgCo(CO)_4$ on CFP was proven by the corresponding elemental

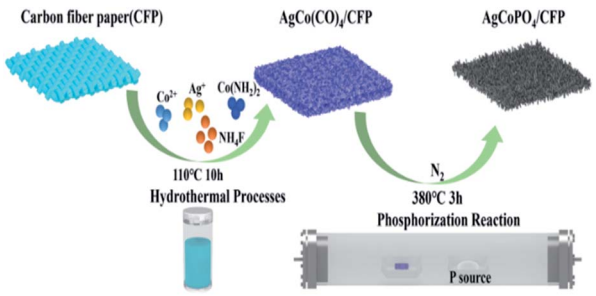

Scheme 1 Schematic illustration of the fabrication process of AgCoPO4/CFP nanorods.

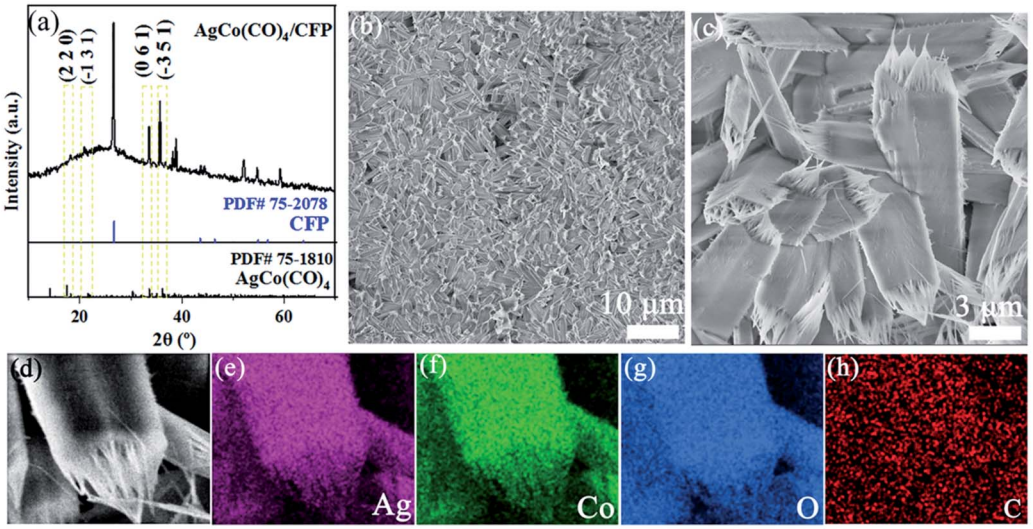

Fig. 1 (a) X-ray diffraction (XRD) patterns of $AgCo(CO)_4$/CFP. (b and c) SEM images of nanorods $AgCo(CO)_4$/CFP at different magnifications. (d) Scanning electron microscope (SEM) images of magnified top of nanorods $AgCo(CO)_4$/CFP. (e–h) Energy dispersive X-ray spectroscopy (EDS) elemental mapping of Ag (purple) (e), Co (green) (f), O (blue) (g) and C (red) (h).

mapping images of Co, Ag, O, and C elements (Fig. 1d–h and S1†).

After phosphorization, the main diffraction peaks were consistent with the pattern of $AgCoPO_4$. The main diffraction peaks at 14.2°, 25.2°, 30.5°, 35.8° and 38.3° can be assigned to the (0 0 1), (0 −3 1), (−2 0 2), (0 1 2), and (−2 1 2) planes of $AgCoPO_4$ (PDF#83-1628) (Fig. 2a). The corresponding peaks of CFP matched well with standard cards. These results demonstrated that $AgCo(CO)_4$/CFP precursor had been transformed into $AgCoPO_4$/CFP after phosphorization. Fig. 2b and c showed that the $AgCoPO_4$/CFP nanostructure obtained by thermal phosphorization. It was composed of randomly oriented nanorods with a regular rhomboid structure at the top and a rhomboid side length was 1.1 μm. The whisker structure on

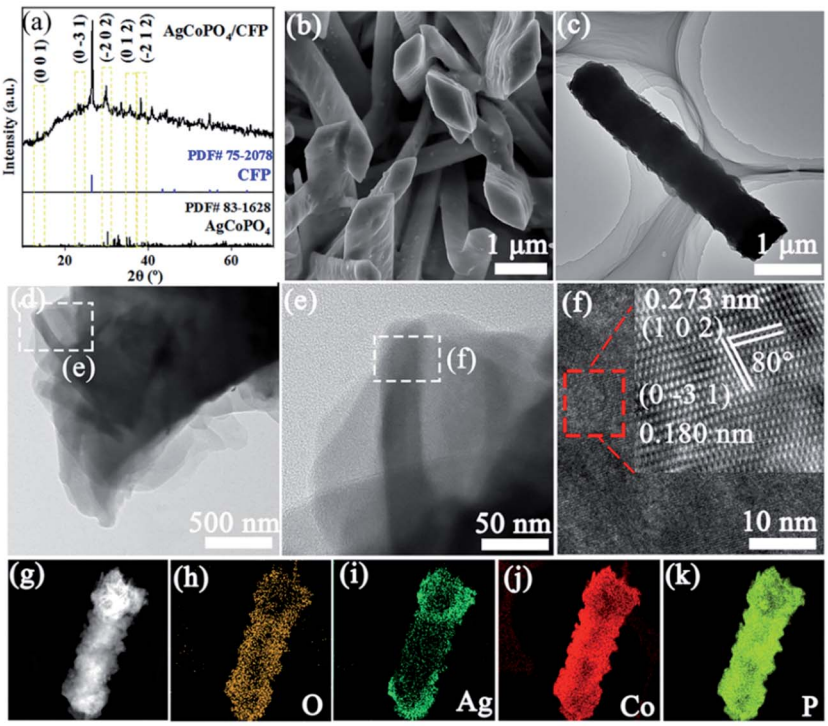

Fig. 2 (a) XRD patterns of $AgCoPO_4$/CFP. (b) SEM images of $AgCoPO_4$/CFP. (c–e) TEM images at different magnifications. (f) HRTEM micrograph. (g–k) Energy dispersive X-ray spectroscopy (EDS) elemental mapping of O (orange) (h), Ag (green) (i), Co (red) (j), and P (chartreuse) (k).

tip of the precursor nanorods was transformed into a smooth diamond tip after phosphorization (Fig. 2b, c and S2†). The change had little effect on the thickness and width of nanorods (Fig. S3†). Transmission electron microscopy (TEM) and high resolution TEM (HRTEM) images of $AgCoPO_4$/CFP revealed the edge of nanorods and well-resolved interplanar distance between faces of the lattice fringes of 0.273 and 0.180 nm, which were indexed to the (1 0 2) and (0 −3 1) plane, and their facet angle was 80.0° (Fig. 2d–f). High magnification element plotting showed that O (Fig. 2h), Ag (Fig. 2i), Co (Fig. 2j), and P (Fig. 2k) were evenly distributed on the whole nanorods.

3.2 Electrochemical performances of $AgCoPO_4$/CFP

Linear sweep voltammetry (LSV) measurements in a three-electrode system (reference electrode: Hg/HgO electrode, counter electrode: carbon electrode) were performed to study the HER properties of the prepared materials. The HER activities of the catalyst with various Co : Ag ratios were firstly tested. The HER catalytic activity was related to silver loading, where the catalytic activity reached the highest performance at the Co : Ag mole ratio of 9 : 1 (Fig. 3a). After determining the optimal ratio (Co : Ag = 9 : 1), we performed linear sweep voltammetry (LSV) measurements to study the HER properties of $AgCo(CO)_4$/CFP, $AgCoPO_4$/CFP and Pt–C/CFP samples in 1 M NaOH electrolyte. As expected, at 10 mA cm^{-2}, Pt–C/CFP showed an overpotential (η) of about 0 mV (*vs.* RHE), which was consistent with the reported value.[10–12] $AgCo(CO)_4$/CFP showed poor activity with an overpotential of about 250 mV. The performance of $AgCoPO_4$/CFP could be greatly improved, for which a current density of 10 mA cm^{-2} only needed an overpotential of 32 mV (Fig. 3b). It was better than most phosphate catalysts in alkaline medium (Tables S1 and S2†). A plot known as the Tafel plot using the logarithmic relationship between η and current density is commonly used to assess electrode performance. The Tafel slope was considered as the growth ratio of the current to the overpotential, mainly determined by the transfer coefficient. Hereby, from the LSV polarization curve we got the Tafel slope in Fig. 3c. The experimental data of all tested catalysts was consist with the Tafel equation $\eta = b \log(j + a)$, where b was the Tafel slope and j was the current density in different overpotential ranges.[32,33] The as-obtained $AgCoPO_4$/CFP possessed a Tafel slope of 34.4 mV dec^{-1}, which was close to that of Pt/C (30.0 mV dec^{-1}), greatly lower than those of $AgCo(CO)_4$/CFP (237.9 mV dec^{-1}) and CFP (447.8 mV dec^{-1}), suggesting that the kinetics toward the HER was greatly improved (Fig. 3c).

In order to further study the high HER activity of $AgCoPO_4$/CFP nanorods, the reaction resistance was studied by electrochemical impedance spectroscopy (EIS), which reflected the charge transfer ability of the electrocatalyst. EIS was operated at the fixed voltage of 0.55 V (Fig. 3d and S4†). R_s represents ohm resistance, and R_{ct} represents charge transfer resistance between $AgCoPO_4$/CFP and electrolyte interface. Nyquist plots showed that $AgCoPO_4$/CFP presented lower semicircle diameter

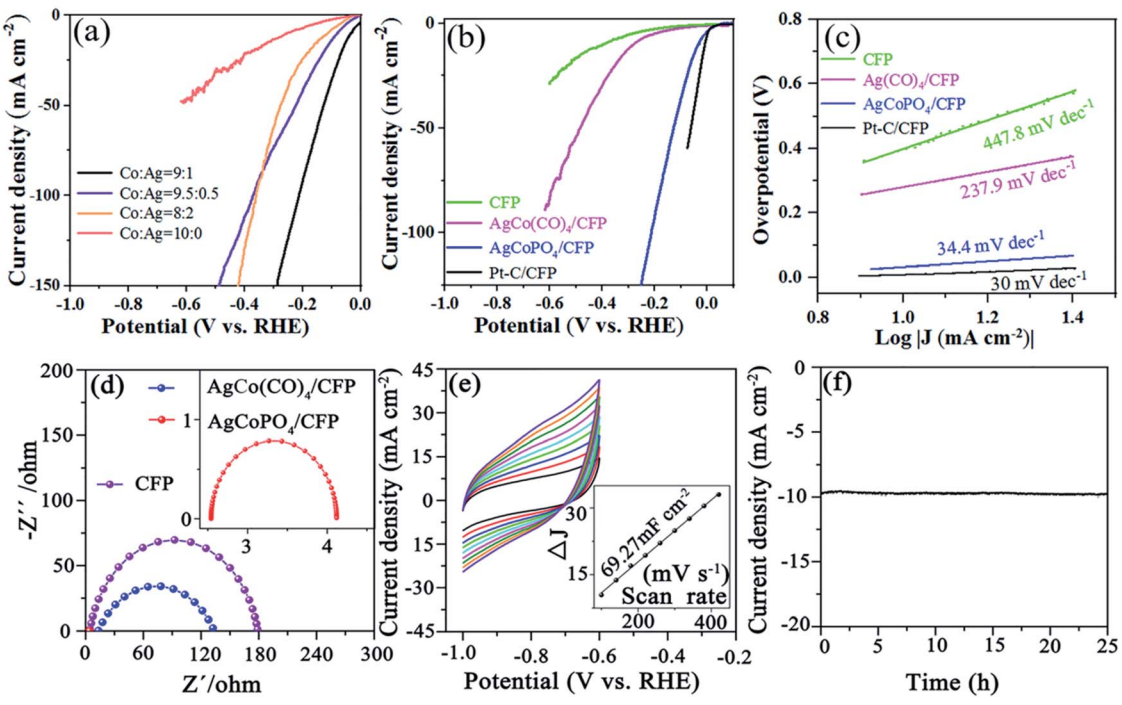

Fig. 3 (a) Hydrogen evolution reaction (HER) properties: polarization curves for Co : Ag/CFP (Co : Ag = 9 : 1, 9.5 : 0.5, 8 : 2, 10 : 0) in 1 M NaOH with a scan rate of 5 mV s^{-1}. (b) Polarization curves without iR compensation for $AgCoPO_4$/CFP and $AgCo(CO)_4$/CFP and Pt–C/CFP. (c) Tafel plot extracted from the corresponding polarization curves with *iR* compensation. (d) Nyquist plots of the $AgCo(CO)_4$/CFP and CFP with an applied bias of 0.4 V, inset is $AgCoPO_4$/CFP. (e) Vyclic voltammetry (CV) scans for $AgCoPO_4$/CFP nanorod structure in 1 M NaOH and capacitive current at −0.8 V as a function of the scan rate. (f) *I*–*t* curves of $AgCoPO_4$/CFP for 25 h at −0.032 V in the cathode.

than that of $AgCo(CO)_4$/CFP and CFP, indicative of the improved charge transfer property of the $AgCoPO_4$/CFP electrode.

Electrochemical active surface area (ECSA) is an effective method to estimate the relative activity of electrocatalysts. CV was used to measure the double-layer capacitance (C_{dl}) between −1.0 and −0.6 V and to evaluate the ECSA.[34–36] As shown in Fig. 3e, the C_{dl} of $AgCoPO_4$/CFP nanorods was 69.27 mF cm^{-2}, which was larger than that of $AgCo(CO)_4$/CFP (11.56 mF cm^{-2}) (Fig. S5†), suggesting that the rod-like nanostructures had more active sites for contact with electrolyte after thermal phosphorization. In addition, it can be seen from the current–time (I–t) curve that $AgCoPO_4$/CFP electrode's catalytic performance showed little change after continuous operation for 25 h (Fig. 3f), indicating that the $AgCoPO_4$/CFP electrode had good stability in 1.0 M NaOH solution.

3.3 The mechanism of the excellent catalytic performance

In order to explore the mechanism for the excellent catalytic performance of $AgCoPO_4$/CFP, the hydrophilicity, chemical environment and corresponding electronic states of the catalyst before and after hydrogen evolution reaction were thoroughly discussed. The contact angle of $AgCoPO_4$ with water was 32.3°. However, the contact angle of CFP with water was 145.9°. Through the contact angle measurements, it was proved that the surface wettability of the CFP was enhanced (Fig. 4a–c). In addition to the surface wettability, the introduction of phosphate is also very important for improving the catalytic performance of HER. Although the precursor $AgCo(CO)_4$ showed good wettability, the catalytic effect was not ideal. Not only did the introduction of phosphate group act as a proton acceptor, facilitating the oxidation of the metal species, but also it promoted metal synergistic catalysis and further facilitated hydrogen evolution reaction.[37,38] The decent surface wettability of $AgCoPO_4$/CFP was good for the adsorption of electrolyte on the electrode surface, and further promoted the hydrogen precipitation.

The chemical states of $AgCoPO_4$/CFP and surface composition were analyzed by XPS before and after HER (Fig. S6†). Two doublets can be observed before and after alkaline HER reaction. The two peaks at binding energies of 374.4 and 368.4 eV can be assigned to Ag $3d_{3/2}$ and $3d_{5/2}$.[39] According to the calculation of peak area, Ag^1 : Ag^0 (area ratio) increased markedly from 1.29 to 1.45 (Fig. 5a). Especially, the binding energy also changed greatly, indicating that the coulomb or

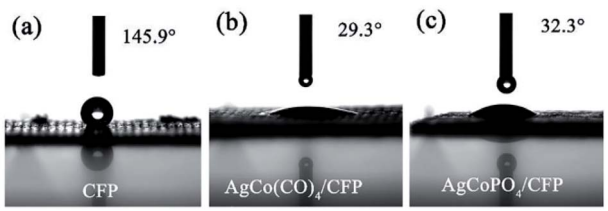

Fig. 4 Contact angle measurements of (a) CFP (b) $AgCo(CO)_4$/CFP and (c) $AgCoPO_4$/CFP.

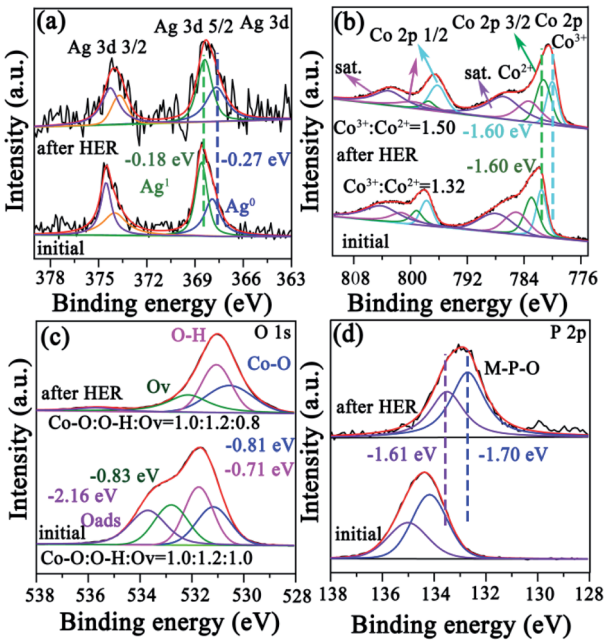

Fig. 5 The XPS spectra of (a) Ag 3d; (b) Co 2p; (c) O 1s; (d) P 2p.

polarographic interaction between Ag and Co led to the increase of electron transfer.[28,40]

Fig. 5b showed the Co 2p spectrum had high resolution XPS and Co $2p_{3/2}$ peaks at 782.3 eV, which were assigned to Co^{3+} and Co^{2+}. Small peaks located at 783.5 eV and 786.9 eV are designated as satellite peaks.[41,42] The ratio of Co^{3+} and Co^{2+} for $AgCoPO_4$/CFP was about 1.32 before the reaction, and it changed to 1.50 after the reaction for 25 h. Thus, the Co on the surface was oxidized to a higher state during HER, which favorable for HER. This can also be confirmed from the activation process of CV curves. The peak of the oxidation from Co^{2+} to Co^{3+} appeared near 0.3 V and 1.25 V.[43–47] Compared with the raw material at the Co : Ag mole ratio of 10 : 0, more obvious oxidation peak appeared. When Ag was introduced into the material, the new peak value in the vicinity of 1.25–1.5 V belonged to the oxidation from Ag to Ag^+. The high valence state of metal played a major role in the catalytic reaction, promoting the rapid progress of catalytic reaction (Fig. S7†). The high resolution XPS spectra showed three oxygen components of O 1s: oxygen within a metal oxide environment (Co–O at 530.6 eV and 530.8 eV),[48,49] oxygen in phosphate environment (O–H at 531.4 eV) and oxygen vacancy (Ov at 532.5 eV).[50,51] Before the alkaline HER, the oxygen in different states was Co–O : O–H : Ov = 1 : 1.2 : 1.0, but it changed to Co–O : O–H : Ov = 1 : 1.2 : 0.8 after alkaline HER (Fig. 5c). The peak analysis after fitting of P 2p displayed different P–O bindings (PO_4^{3-} at 135.0 eV, M–P–O (M = Co, Cu) at 133.6–134.2 eV). Here, the PO_4^{3-} belonged to the $AgCoPO_4$ phase (Fig. 5d).[52,53]

The TEM images after alkaline recycling were presented in Fig. 6a. They possessed similar nanorod-like structure, which indicated that $AgCoPO_4$/CFP after alkaline recycling still possessed intrinsic stability. HRTEM image showed a nanorod-

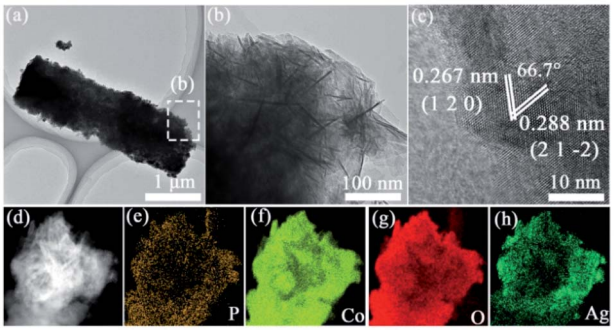

Fig. 6 Structural and compositional evolution of the $AgCoPO_4$/CFP electrode after HER: (a and b) TEM images at different magnifications. (c) HRTEM images. (d–h) Energy dispersive X-ray spectroscopy (EDS) elemental mapping of P (orange) (e), Ag (chartreuse) (f), O (red) (g) and Ag (green) (h).

like structure of $AgCoPO_4$/CFP on the edge (Fig. 6b). Moreover, the lattice spacing of 0.267 and 0.288 nm belonged to (1 2 0) and (2 1 −2) planes in $AgCoPO_4$, their facet angle was 66.7° (Fig. 6c). Furthermore, the corresponding elemental mappings demonstrated the uniform distribution of Ag, Co, P, and O elements in $AgCoPO_4$ (Fig. 6d–h). Therefore, the change of hydrophilicity and surface electronic structure caused by the synergistic effect of bimetal and the exposure of catalytic active sites contributed to the high catalytic activity of $AgCoPO_4$/CFP in HER.

3.4 Excellent urea oxidation reaction (UOR) activity

The traditional catalysts for HER and OER are RuO_2 and Pt on the basis of extremely rare and expensive precious metals.[33] It is important to develop alternative electrolytic cells. $AgCoPO_4$/CFP not merely had good HER catalytic activity. Urea is notorious for environmental problems, but it is a promising option for producing H_2 in electrolytic cell.[54] After UOR, urea decomposes into inert N_2 and carbon dioxide. When UOR is applied to replace OER, energy consumption and security problems can be solved.[55] We also tested different UOR and OER processes with different proportions of Ag, and the results proved that Co : Ag = 9 : 1 ($AgCoPO_4$/CFP) had the best performance (Fig. S8†). The electrochemical properties of $AgCoPO_4$/CFP on OER and UOR were tested respectively in 0.5 M urea + 1.0 M NaOH electrolyte. The electrode potential of $AgCoPO_4$/CFP for UOR at 15 mA cm^{-2} was 1.43 V (Fig. 7a), which had a low Tafel slope at 49.1 mV dec^{-1} (Fig. 7b). At 10 mA cm^{-2}, the potential of UOR is 180 mV lower than OER, the energy required for urea oxidation was significantly lower than that for water oxidation. We had developed an electrolytic cell using $AgCoPO_4$/CFP as anode and cathode electrocatalysts (Fig. S9† and 7a). As we can see in Fig. 7c, the cell voltage needed by the $AgCoPO_4$/CFP||$AgCoPO_4$/CFP electrolyzer in 1 M NaOH + 0.5 M urea at 10 mA cm^{-2} was 1.45 V (Fig. 7c), lower than that of water splitting (1.54 V), which proved that urea oxidation assisting hydrogen production can reduce the energy consumption of hydrogen production. In addition, to evaluate the stability of $AgCoPO_4$/CFP in HER-UOR cell, a constant current test was performed. Fig. 6d showed that after 18 h of electrolysis, the cell voltage had no obvious attenuation, indicating that $AgCoPO_4$/CFP had good durability as the bifunctional electrode for urea-assisted electrochemical hydrogen production.

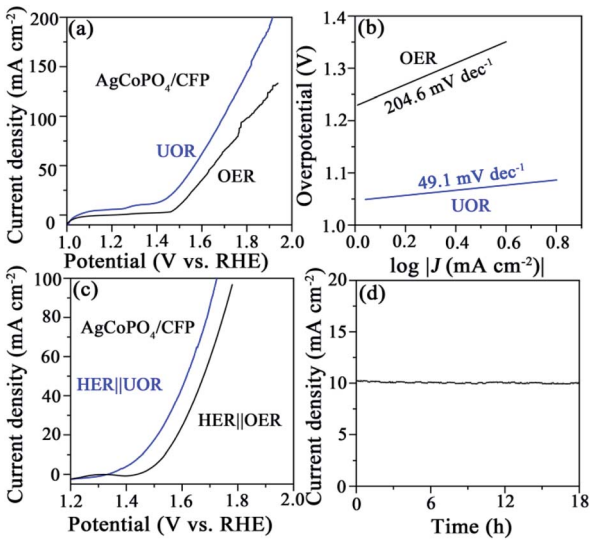

Fig. 7 (a) LSV curves of $AgCoPO_4$/CFP for OER and UOR. (b) Tafel plots. (c) Polarization curves of $AgCoPO_4$/CFP||$AgCoPO_4$/CFP electrolyzer in 1 M NaOH and 1 M NaOH + 0.5 M Urea. (d) The current–time curve of $AgCoPO_4$/CFP||$AgCoPO_4$/CFP electrolyzer at a constant current density of 10 mA cm^{-2} in 1 M NaOH + 0.5 M urea.

4. Conclusions

In this work, a simple and controllable self-supported method was used for the synthesis of $AgCoPO_4$/CFP nanorods. The synthesized $AgCoPO_4$/CFP nanorods exhibited excellent alkaline hydrogen evolution catalytic performance and remarkable long-term durability. Under 10 mA cm^{-2} of 1 M NaOH, it showed an overpotential decrease of 32 mV and the Tafel slope was 34.4 mV dec^{-1}. The rod-like nanostructures had significant electrical conductivity, which promoted the complete contact between the active site and electrolyte, and further accelerated the gas desorption process through the conversion of hydrophobic and hydrophilic properties. It also could be used as the anode and cathode of the electrolytic cell and had decent overall water separation performance. This study on the structure–performance relationship shed light on the controllable design of low-cost and efficient transition metal phosphorylation catalysts in the future. In addition, the $AgCoPO_4$/CFP nanorods synthesis method mentioned in this study had low requirement preparation conditions, which holds the promise of achieving relatively large-scale industrial production and applying it to emerging energy technologies.

Conflicts of interest

There are no conflicts to declare.

Acknowledgements

This work was supported by the National Natural Science Foundation of China (No. 22174047).

Notes and references

1 H. A. Gasteiger and N. M. Markovic, Just a dream-or future reality?, *Science*, 2009, **48**, 324.

2 Q. Fu, T. Wu, G. Fu, T. Gao, J. Han, T. Yao, Y. Zhang, W. Zhong, X. Wang and B. Song, Skutterudite-type ternary $Co_{1-x}Ni_xP_3$ nanoneedle array electrocatalysts for enhanced hydrogen and oxygen evolution, *ACS Energy Lett.*, 2018, **3**, 1744–1752.

3 S. A. Chala, M. C. Tsai, W. N. Su, K. B. Ibrahim, A. D. Duma, M. H. Yeh, C. Y. Wen, C. H. Yu, T. S. Chan, H. Dai and B. J. Hwang, Site activity and population engineering of NiRu-layered double hydroxide nanosheets decorated with silver nanoparticles for oxygen evolution and reduction reactions, *ACS Catal.*, 2019, **9**, 117–129.

4 Z. W. Seh, J. Kibsgaard, C. F. Dickens, I. b. Chorkendorff, J. K. Nørskov and T. F. Jaramillo, Combining theory and experiment in electrocatalysis: Insights into materials design, *Science*, 2017, **355**, 6321.

5 Q. Gong, Y. Wang, Q. Hu, J. Zhou, R. Feng, P. N. Duchesne, P. Zhang, F. Chen, N. Han, Y. Li, C. Jin, Y. Li and S. T. Li, Ultrasmall and phase-pure W_2C nanoparticles for efficient electrocatalytic and photoelectrochemical hydrogen evolution, *Nat. Commun.*, 2016, **7**, 13216.

6 N. S. Lewis and D. G. Nocera, Powering the planet: Chemical challenges in solar energy utilization, *Proc. Natl. Acad. Sci. U.S.A.*, 2006, **103**, 15729.

7 H. B. Gray, Powering the planet with solar fuel, *Nat. Chem.*, 2009, **1**, 7.

8 H. Vrubel and X. L. Hu, Molybdenum boride and carbide catalyze hydrogen evolution in both acidic and basic solutions, *Angew. Chem., Int. Ed.*, 2012, **51**, 12875–12878.

9 X. D. Jia, Y. F. Zhao, G. B. Chen, L. Shang, R. Shi, X. F. Kang, G. I. N. Waterhouse, L. Z. Wu, C. H. Tung and T. R. Zhang, Ni_3FeN nanoparticles derived from ultrathin NiFe-Layered double hydroxide nanosheets: an efficient overall water splitting electrocatalyst, *Adv. Energy Mater.*, 2016, **6**, 1502585.

10 H. Yin, S. Zhao, K. Zhao, A. Muqsit, H. Tang, L. Chang, H. Zhao, Y. Gao and Z. Tang, Ultrathin platinum nanowires grown on single-layered nickel hydroxide with high hydrogen evolution activity, *Nat. Commun.*, 2015, **6**, 6430.

11 Y. Wang, L. Chen, X. Yu, Y. Wang and G. Zheng, Superb alkaline hydrogen evolution and simultaneous electricity generation by Pt-decorated Ni_3N nanosheets, *Adv. Energy Mater.*, 2017, **7**, 1601390.

12 X. Han, X. Ling, D. Yu, D. Xie, L. Li, S. Peng, C. Zhong, N. Zhao, Y. Deng and W. Hu, Atomically dispersed binary Co-Ni sites in nitrogen-doped hollow carbon nanocubes for reversible oxygen reduction and evolution, *Adv. Mater.*, 2019, **31**, 1905622.

13 H. B. Wu, B. Y. Xia, L. Yu, X. Y. Yu and X. W. Lou, Porous molybdenum carbide nano-octahedrons synthesized via confined carburization in metal–organic frameworks for efficient hydrogen production, *Nat. Commun.*, 2015, **6**, 6512.

14 N. M. Marković, B. N. Grgur and P. N. Ross, Temperature-dependent hydrogen electrochemistry on platinum low-index single-crystal surfaces in acid solutions, *J. Phys. Chem. B*, 1997, **101**, 5405–5413.

15 X. X. Zou and Y. Zhang, Noble metal-free hydrogen evolution catalysts for water splitting, *Chem. Soc. Rev.*, 2015, **44**, 5148–5180.

16 S. M. Li, K. Kang and H. Jang, Environmental friendly synthesis of hierarchicalmesoporous platinum nanoparticles templated by fucoidan biopolymer for enhancedhydrogen evolution reaction, *J. Mater. Sci. Lett.*, 2020, **46**, 185–190.

17 D. H. Ha, B. Han, M. Risch, L. Giordano, C. Yao, P. Karayaylali and Y. Shao, Activity and stability of cobalt phosphides for hydrogen evolution upon water splitting, *Nano Energy*, 2016, **29**, 37–45.

18 X. Yang, A. Y. Lu, Y. Zhu, M. N. Hedhili, S. Min, K. W. Huang, Y. Han and L. J. Li, CoP nanosheet assembly grown on carbon cloth: A highly efficient electrocatalyst for hydrogen generation, *Nano Energy*, 2015, **15**, 634–641.

19 H. Zheng, Y. Li, Y. Wang and P. Gao, Fabrication of $Co(PO_3)_2$@NPC/MoS_2 heterostructures for enhanced electrocatalytic hydrogen evolution, *J. Alloys Compd.*, 2022, **894**, 162411.

20 Y. Wang, L. Chen, X. Yu, Y. Wang and G. Zheng, Superb alkaline hydrogen evolution and simultaneous electricity generation by Pt-decorated Ni_3N nanosheets, *Adv. Energy Mater.*, 2017, **7**, 1601390.

21 Q. Q. Chen, X. Yang, C. C. Hou, K. Li and Y. Chen, Inlay of ultrafine Ru nanoparticles into a self-supported $Ni(OH)_2$ nanoarray for hydrogen evolution with low overpotential and enhanced kinetics, *J. Mater. Chem. A.*, 2019, **7**, 11062–11068.

22 S. A. Chala, M. C. Tsai, W. N. Su, K. B. Ibrahim, A. D. Duma, M. H. Yeh, C. Y. Wen, C. H. Yu, T. S. Chan, H. Dai and B. J. Hwang, Site activity and population engineering of NiRu-layered double hydroxide nanosheets decorated with silver nanoparticles for oxygen evolution and reduction reactions, *ACS Catal.*, 2019, **9**, 117–129.

23 L. M. Leng, J. Li, X. Y. Zeng, X. L. Tian, H. Y. Song, Z. M. Cui, T. Shu, H. S. Wang, J. W. Ren and S. J. Liao, Enhanced cyclability of LiO_2 batteries with cathodes of Ir and MnO_2 supported on well-defined TiN arrays, *Nanoscale*, 2018, **10**, 2983–2989.

24 X. Sun, C. Chen, S. Liu, S. Hong, Q. Zhu, Q. Qian, B. Han, J. Zhang and L. Zheng, Aqueous CO_2 reduction with high efficiency using α-$Co(OH)_2$-supported atomic Ir electrocatalysts, *Angew. Chem.*, 2019, **131**, 4717–4721.

25 X. Zhao, P. Gao, Y. Yan, X. Li, Y. Xing, H. Li, Z. Peng, J. Yang and J. Zeng, Gold atom-decorated $CoSe_2$ nanobelts with engineered active sites for enhanced oxygen evolution, *J. Mater. Chem. A.*, 2017, **5**, 20202–20207.

26 Y. Hou, Y. Liu, R. Gao, Q. Li, H. Guo, A. Goswami, R. Zboril, M. B. Gawande and X. Zou, Spontaneous synthesis of silver-nanoparticle-decorated transition-metal hydroxides for

enhanced oxygen evolution reaction, *Angew. Chem., Int. Ed.*, 2020, **59**, 7245.

27 R. Liu, K. Ye, Y. Gao, W. Zhang, G. Wang and D. Cao, Ag supported on carbon fiber cloth as the catalyst for hydrazine oxidation in alkaline medium, *Electrochim. Acta*, 2015, **186**, 239–244.

28 H. Xu, X. Niu, Z. Liu, M. Sun, Z. Liu, Z. Tian, X. Wu, B. Huang, Y. Tang and C. Yan, Highly controllable hierarchically porous Ag/Ag_2S heterostructure by cation exchange for efficient hydrogen evolution, *Small*, 2021, **17**, 2103064.

29 Z. Cui, Y. Li, G. Fu, X. Li and J. B. Goodenough, Robust Fe_3Mo_3C supported IrMn clusters as highly efficient bifunctional air electrode for metal–air battery, *Adv.Mater.*, 2017, **29**, 1702385.

30 Y. Tan, H. Wang, P. Liu, C. Cheng, F. Zhu, A. Hirata and M. Chen, 3D nanoporous metal phosphides toward high-efficiency electrochemical hydrogen production, *Adv. Mater.*, 2016, **28**, 2951.

31 E. J. Popczun, C. G. Read, C. W. Roske, N. S. Lewis and R. E. Schaak, Highly active electrocatalysis of the hydrogen evolution reaction by cobalt phosphide nanoparticles, *Angew. Chem., Int. Ed.*, 2014, **53**, 5427.

32 Y. Jiao, Y. Zheng, M. T. Jaroniec and S. Z. Qiao, Design of electrocatalysts for oxygen- and hydrogen-involving energy conversion reactions, *Chem. Soc. Rev.*, 2015, **44**, 2060–2086.

33 H. S. Cao, Y. Xie, H. L. Wang, F. Xiao, A. P. Wu, L. Li, Z. K. Xu, N. Xiong and K. Pan, Flower-like CoP microballs assembled with (002) facet nanowires via precursor route: Efficient electrocatalysts for hydrogen and oxygen evolution, *Electrochim. Acta*, 2018, **259**, 830–840.

34 T. Wu, M. Pi, D. Zhang and S. Chen, 3D structured porous CoP_3 nanoneedle arrays as an efficient bifunctional electrocatalyst for the evolution reaction of hydrogen and oxygen, *J. Mater. Chem. A.*, 2016, **4**, 14539–14544.

35 Y. P. Zhu, Y. P. Liu, T. Z. Ren and Z. Y. Yuan, Self-supported cobalt phosphide mesoporous nanorod arrays: A flexible and bifunctional electrode for highly active electrocatalytic water reduction and oxidation, *Adv. Funct. Mater.*, 2015, **25**, 7337–7347.

36 H. Wu, X. Lu, G. Zheng and G. W. Ho, Topotactic engineering of ultrathin 2D nonlayered nickel selenides for full water electrolysis, *Adv. Energy Mater.*, 2018, **8**, 1702704.

37 Y. Li and C. Zhao, Enhancing water oxidation catalysis on a synergistic phosphorylated NiFe hydroxide by adjusting catalyst wettability, *ACS Catal.*, 2017, **7**, 2535–2541.

38 X. Zhang and X. Yu, Hosphide/Carbon nanotube hybrids as pH-universal electrocatalysts for hydrogen evolution reaction, *Adv. Funct. Mater.*, 2018, **28**, 1706523.

39 C. V. Babaahmadi, M. Montazer and W. Gao, Low temperature welding of graphene on PET with silver nanoparticles producing higher durable electro-conductive fabric, *Carbon*, 2017, **118**, 443.

40 X. Song, Z. Y. Zhao, X. X. Sun, Y. H. Zhou, Y. Wang and D. B. Wang, In situ growth of Ag nanodots decorated Cu_2O porous nanobelts networks on copper foam for efficient HER electrocatalysis, *Small*, 2019, **15**, 1804268.

41 Y. Y. Feng, T. Zhang, J. H. Zhang, H. Fan, C. He and J. X. Song, 3D 1T-MoS_2/CoS_2 heterostructure via interface engineering for ultrafast hydrogen evolution reaction, *Small*, 2020, **16**, 2002850.

42 X. Chen, M. Cheng, D. Chen and R. Wang, Shape-Controlled Synthesis of Co_2P Nanostructures and Their Application in Supercapacitors, *ACS Appl. Mater. Interfaces*, 2016, **8**, 3892–3900.

43 Y. Pan, Y. Liu and C. Liu, Metal doping effect of the MCo_2P/Nitrogen-doped carbon nanotubes (M = Fe, Ni, Cu) hydrogen evolution hybrid catalysts, *ACS Appl. Mater. Interfaces*, 2016, **8**, 13890–13901.

44 R. Vittal and H. Gomathi, Prabhakara Rao, Derivatised nickel and cobalt oxide modified electrodes: effect of surfactant, *Electroanal. Chem.*, 2001, **497**, 47.

45 C. Barbem, G. A. Planes and M. C. Miras, Redox coupled ion exchange in cobalt oxide films, *Electrochem. Cotmmm.*, 2001, **3**, 113.

46 I. G. Casella, Electrodeposition of cobalt oxide films from carbonate solutions containing Co(II)–tartrate complexes, *Elearoanal. Chem.*, 2002, **520**, 119.

47 I. G. Casella and M. J. Gatta, Study of the electrochemical deposition and properties of cobalt oxide species in citrate alkaline solutions, *Electroanal.Chem.*, 2002, **534**, 31.

48 P. Elumalai, H. N. Vasan and N. Munichandmiah, Electrochemical studies of cobalt hydroxide — an additive for nickel electrodes, *Power Sources*, 2001, **93**, 201.

49 Y. M. Xia, Z. M. He, K. J. Hu, B. Tang, J. B. Su, Y. Liu and X. P. Li, Fabrication of n-$SrTiO_3$/p-Cu_2O heterojunction composites with enhanced photocatalytic performance, *J. Alloy Compd.*, 2018, **753**, 356.

50 C. Yuan, J. Li, L. Hou, X. Zhang, L. Shen and X. Lou, Ultrathin mesoporous $NiCo_2O_4$ nanosheets supported on Ni foam as advanced electrodes for supercapacitors, *Adv. Funct. Mater.*, 2012, **22**, 4592–4597.

51 H. Cao, Z. Li, Y. Xie, F. Xiao, H. Wang, X. Wang, K. Pan and A. Cabot, Hierarchical CoP nanostructures on nickel foam as efficient bifunctional catalysts for water splitting, *ChemSusChem*, 2021, **14**, 1094.

52 H. Q. Zhou, F. Yu, J. Y. Sun, R. He, S. Chen, C. W. Chu and Z. F. Ren, Highly active catalyst derived from a 3D foam of $Fe(PO_3)_2/Ni_2P$ for extremely efficient water oxidation, *Proc. Natl. Acad. Sci. U.S.A.*, 2017, **114**, 5607–5611.

53 Y. Li, Z. Wang, J. Hu, S. Li, Y. Du, X. Han and P. Xu, Metal–organic frameworks derived interconnected bimetallic metaphosphate nanoarrays for efficient electrocatalytic oxygen evolution, *Angew. Chem.*, 2014, **126**, 6828–6832.

54 S. Chen, J. Duan, A. Vasileff and S. Z. Qiao, Size fractionation of Two-dimensional sub-nanometer thin manganese dioxide crystals towards superior urea electrocatalytic conversion, *Angew. Chem.*, 2016, **55**, 3804–3808.

55 S. K. Geng, Y. Zheng, S. Q. Li, H. Su, X. Zhao, J. Hu, H. B. Shu, M. Jaroniec, P. Chen, Q. H. Liu and S. Z. Qiao, Nickel ferrocyanide as a high-performance urea oxidation electrocatalyst, *Nat. Energy.*, 2021, **6**, 904–912.